Structure of a prereaction complex between the nerve agent sarin, its biological target acetylcholinesterase, and the antidote HI-6

Anders Allgardsson[a,1], Lotta Berg[b,1], Christine Akfur[a], Andreas Hörnberg[c], Franz Worek[d], Anna Linusson[b,2], and Fredrik J. Ekström[a,2]

[a]Department of CBRN Defence and Security, Swedish Defence Research Agency, SE-90182 Umea, Sweden; [b]Department of Chemistry, Umeå University, SE-90187 Umea, Sweden; [c]SP Processum AB, SE-891 22 Ornskoldsvik, Sweden; and [d]Department of Toxicological Enzymology, Bundeswehr Institute of Pharmacology and Toxicology, 80937 Munich, Germany

Edited by Joel L. Sussman, Weizmann Institute of Science, Rehovot, Israel, and accepted by the Editorial Board March 29, 2016 (received for review November 26, 2015)

Organophosphorus nerve agents interfere with cholinergic signaling by covalently binding to the active site of the enzyme acetylcholinesterase (AChE). This inhibition causes an accumulation of the neurotransmitter acetylcholine, potentially leading to overstimulation of the nervous system and death. Current treatments include the use of antidotes that promote the release of functional AChE by an unknown reactivation mechanism. We have used diffusion trap cryocrystallography and density functional theory (DFT) calculations to determine and analyze prereaction conformers of the nerve agent antidote HI-6 in complex with *Mus musculus* AChE covalently inhibited by the nerve agent sarin. These analyses reveal previously unknown conformations of the system and suggest that the cleavage of the covalent enzyme–sarin bond is preceded by a conformational change in the sarin adduct itself. Together with data from the reactivation kinetics, this alternate conformation suggests a key interaction between Glu202 and the *O*-isopropyl moiety of sarin. Moreover, solvent kinetic isotope effect experiments using deuterium oxide reveal that the reactivation mechanism features an isotope-sensitive step. These findings provide insights into the reactivation mechanism and provide a starting point for the development of improved antidotes. The work also illustrates how DFT calculations can guide the interpretation, analysis, and validation of crystallographic data for challenging reactive systems with complex conformational dynamics.

acetylcholinesterase | density functional theory | crystallography | nerve agent | reactivation

A protein's structure can be described in terms of a multidimensional energy landscape where different conformational states are separated by energy barriers (1, 2). The protein moves constantly across this landscape because of thermally driven fluctuations and interactions with ligands and substrates. The motions and dynamics of proteins are typically studied using techniques, such as NMR and/or molecular dynamics simulations. However, conformational ensembles are also often encountered in X-ray crystallography, enabling structural analysis of the spatial component of dynamics (3). Although such ensembles of conformers can be critical for understanding a protein's function, they can also generate electron density maps that are difficult to interpret because of spatial averaging. This problem has been encountered in crystallographic studies on enzyme reactivation mediated by nerve agent antidotes (i.e., nucleophilic compounds that are used to treat intoxication by chemical warfare agents, such as sarin, VX, or tabun). Nerve agents potently inhibit the essential cholinergic enzyme acetylcholinesterase (AChE; EC 3.1.1.7) by phosphonylating its catalytic serine residue (Ser203) and therefore, rendering it incapable of hydrolyzing the neurotransmitter acetylcholine (4). This inhibition causes acetylcholine to accumulate, leading to overstimulation of the nervous system and eventually, death. Treatment of nerve agent-inactivated AChE with an antidote causes the release of the functional enzyme and the formation of a phosphonyl oxime (Fig. 1*A*) (4, 5). Although the process has been studied for decades, detailed mechanistic information is still lacking.

We have previously used X-ray crystallography to study the complex between the nerve agent antidote HI-6 and *Mus musculus* acetylcholinesterase (*m*AChE) phosphonylated by the nerve agent sarin (sarin–*m*AChE) (Fig. 1 *B*–*D*) (6). The binary sarin–*m*AChE complex and the ternary complex HI-6•sarin–*m*AChE can undergo (multiple) chemical reactions in solution (Fig. 1*A*) (7, 8) as well as in the crystal phase (9, 10). The addition of HI-6 to the sarin–AChE complex leads to a reaction that cleaves the bond between the oxygen of Ser203 and the phosphorus atom of sarin (Fig. 1*A*) (4, 5, 11). Furthermore, the sarin adduct can undergo a dealkylation reaction, termed "aging," that renders the enzyme resistant to reactivation by HI-6 (7). Because of the system's reactivity, the composition of crystals obtained by trapping the productive complex of sarin–*m*AChE and HI-6 is highly time-dependent, and the crystals inevitably contain several conformers and chemical species. These features make the system particularly challenging to study.

Significance

Enzymatic reactions can be difficult to study using X-ray crystallography, because conformations and reacting species are temporally and spatially averaged, and many reactions proceed to completion before intermediates can be trapped. Here, we describe the combined use of diffusion trap cryocrystallography, density functional theory calculations, and kinetic measurements to investigate the reactivation of the essential cholinergic enzyme acetylcholinesterase by the nerve agent antidote HI-6 after covalent inhibition by the nerve agent sarin. We have determined prereaction conformations of HI-6 and propose that the reactivating cleavage of the enzyme–sarin bond is preceded by a change in the sarin adduct's binding pose. The structures presented in this work will facilitate additional mechanistic analysis and the development of novel antidotes.

Author contributions: A.A., L.B., A.L., and F.J.E. designed research; A.A., L.B., C.A., A.H., F.W., and F.J.E. performed research; A.A., L.B., F.W., A.L., and F.J.E. analyzed data; and A.A., L.B., F.W., A.L., and F.J.E. wrote the paper.

The authors declare no conflict of interest.

This article is a PNAS Direct Submission. J.L.S. is a guest editor invited by the Editorial Board.

Freely available online through the PNAS open access option.

Data deposition: The crystallography, atomic coordinates, and structure factors have been deposited in the Protein Data Bank, www.pdb.org (PDB ID codes 5FPP and 5FPQ).

[1]A.A. and L.B. contributed equally to this work.

[2]To whom correspondence may be addressed. Email: anna.linusson@umu.se or freeks@foi.se.

This article contains supporting information online at www.pnas.org/lookup/suppl/doi:10.1073/pnas.1523362113/-/DCSupplemental.

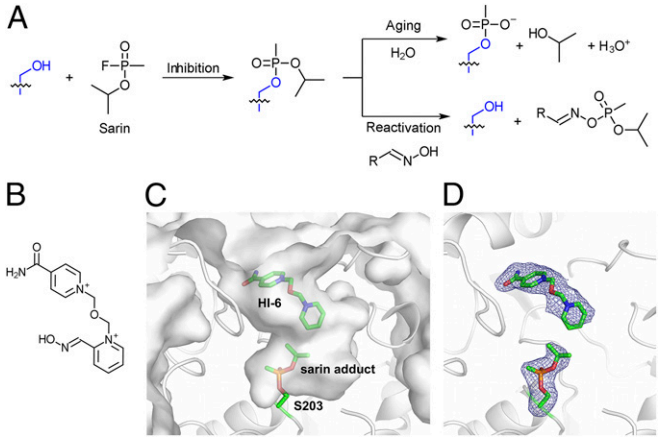

Fig. 1. (*A*) The catalytic S203 (blue) of *m*AChE is phosphonylated by sarin. The adduct is reactive and can undergo multiple chemical reactions. (*B*) The nerve agent reactivator HI-6 binds close to the adduct in (*C*) the deep, narrow, and highly aromatic active site gorge of *m*AChE. (*D*) In previous crystal structures (PDB ID code 2WHP), the *O*-isopropyl of the sarin adduct sterically shields the phosphorus, and the electron density maps do not define the position or conformation of the nucleophilic oxime moiety. Oxygen, nitrogen, and phosphorus are shown in red, blue, and orange, respectively.

Analyses of the previously reported ternary complex [Protein Data Bank (PDB) ID code 2WHP] revealed that HI-6 interacted with the arenes of Tyr124 and Trp286 to form a well-defined sandwich structure and that the sarin *O*-isopropyl moiety adopted a "closed" conformation that sterically shields the phosphorus atom against nucleophilic attack (Fig. 1*C*) (6). However, the electron density maps did not define the conformation or position of the reactive oxime moiety of HI-6, presumably because of spatial averaging (Fig. 1*D*) (6). These findings were supported by molecular dynamics simulations of the system, which revealed significant conformational dynamics of the nucleophilic pyridinium-oxime ring of HI-6 (6). Thus, in addition to the difficulties in defining the oxime moiety, the structure did not reveal how the nucleophile approaches the phosphorus atom of the sarin adduct and could not be used to support a detailed analysis of the reactivation mechanism.

Ligands that are challenging to model in the electron density map are not unique to the system described above (12). For example, a computational method for redefining noise and interpreting weak electron density features revealed a previously hidden conformation of the HIV capsid protein (13). We recently presented a study in which we integrated conventional crystallographic refinement with a quantum chemical cluster approach using implicit dispersion-corrected density functional theory (DFT) calculations to refine and analyze the structure of a complex between *m*AChE and a pair of enantiomeric ligands (14, 15). In conventional crystallographic refinement, the experimental data are supported by molecular mechanics force fields that ensure that the bond lengths and angles of the protein and ligands are realistic (16). However, in the enantiomeric study, the experimental data did not unambiguously define the conformations and intermolecular contacts of the studied complexes. Combining crystallographic data with DFT calculations made it possible to identify low-energy conformations that are chemically plausible and consistent with experimentally derived electron density maps. Here, we describe the use of a similar refinement strategy that combines diffusion trap cryocrystallography and DFT calculations to identify low-energy conformations of the complex between HI-6 and *m*AChE phosphonylated by sarin (sarin–*m*AChE). The structure reveals previously unknown conformations of the system and a plausible preattack coordination of the nucleophile. The mechanistic implications of the structural analysis were investigated using site-directed mutagenesis, studies on the enzyme's reactivation kinetics, and measurements of solvent isotope effects using deuterium oxide.

Results and Discussion

Capturing Low-Energy Intermediates Using a Diffusion Trap Strategy. Reactivation in the crystalline state was investigated in multiple time-dependent soaking experiments. The HI-6 antidote was allowed to diffuse into *m*AChE crystals pretreated with sarin during an incubation period of 1, 2, 3, or 4 min, which was followed by rapid vitrification to trap the conformational states of the crystal. The progress of the reactivation reaction was visualized using electron density maps (specifically, simulated annealing $F_o - F_c$ omit maps), which showed a time-dependent decrease in the intensity around the sarin adduct (Fig. 2*A*). These results show that HI-6–assisted reactivation occurs in the crystalline state at a timescale that can be captured by the diffusion trap experiments.

To improve the sampling of the system and capture prereaction conformational states, we performed over 80 soaking experiments using an HI-6 incubation time of 3 min. The subsequent diffraction experiments yielded nine refined crystal structures with resolutions ranging from 2.2 to 2.7 Å. The system's chemical and structural complexity was clearly shown by the feature-rich electron density maps of nine datasets, which show a common principal density representing the scaffold of HI-6 (Fig. 2*B*). In addition, each of the nine electron density maps had unique features. Of particular interest were two datasets showing interconnected electron density maps corresponding to HI-6 and the sarin adduct—we postulated that the interconnection might make it possible to model the previously missing HI-6 oxime moiety in the 2WHP structure. One dataset was selected for additional refinement (resolution of 2.4 Å) (Fig. 2*C* and Table S1). The data were amenable to conventional crystallographic refinement, generating an initial model

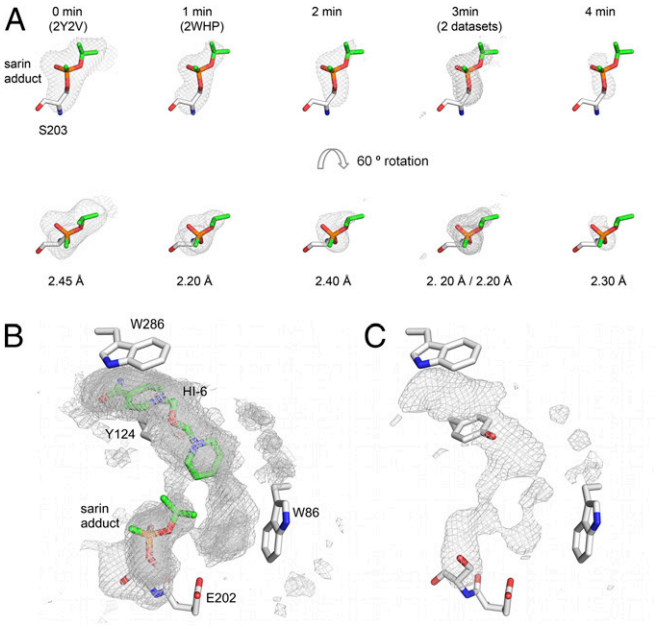

Fig. 2. (*A*) A diffusion trap experiment showing the time-dependent decline in electron density around the sarin adduct. (*B*) A superposition of nine electron density maps from data collected after a 3-min incubation with HI-6. (*C*) The electron density map that was selected for additional analysis and refinement of the ^{3min}HI-6•sarin–*m*AChE structure. The $F_o - F_c$–simulated annealing omit electron density maps are contoured at 3σ. For incubation times of 2–4 min and in *B* and *C*, the coordinates of the previously determined structure of sarin-phosphonylated *m*AChE in complex with HI-6 (PDB ID code 2WHP) are shown as a reference. Oxygen, nitrogen, and phosphorus are shown in red, blue and orange, respectively.

(^{3min}HI-6•sarin–*m*AChE) with a superficially acceptable fit to the electron density map. However, the electron density corresponding to the sarin adduct was weak and partly absent. The weak electron density is likely a consequence of a reduced occupancy because of partial reactivation (Fig. 2*A*), partial aging with loss of the *O*-isopropyl chain (Fig. 1*A*), and/or spatial averaging because of conformational dynamics. Although the data suggest that sarin is bound to Ser203, the electron density maps were considered too weak to allow reliable crystallographic refinement of the adduct. In contrast, the entire HI-6 molecule was defined by electron density, with the *E* and *Z* isomers of the oxime having similar fits. During the initial refinement of ^{3min}HI-6•sarin–*m*AChE, the occupancy was set to 0.3 and 1.0 for sarin and HI-6, respectively. In addition to the density defining HI-6 and the sarin adduct, there were unaccounted positive difference peaks, especially close to the indole ring of Trp86. Despite efforts to model all of the features observed in the active site, the identities of several positive difference peaks remain unclear. This ambiguity is probably because of the temporal and spatial averaging of the system, some of which is attributable to the reactivation reaction (Fig. 1*A*). In addition, the features observed in the vicinity of the indole ring of Trp86 indicate the presence of a ligand, possibly combined with conformational mobility of one or several side chains. These features were more pronounced in the B monomer, revealing an unproductive conformer of the system in which HI-6 is nearly parallel to the indole ring of Trp86 (Fig. S1). Attempts to model the reactivation product, the phosphonylated HI-6, yielded inconclusive results. As a reference, the half-life of phosphonylated HI-6 is short, probably less than 1 s (5). Thus, the timescale of this experiment is not suitable for trapping the phosphonylated HI-6. Other previously reported conformations and/or conjugation states that were considered during the refinement are shown in Fig. S1.

Refinement of Low-Occupancy Conformers. To address the limitations of conventional crystallographic refinement of low-occupancy conformers, we used a quantum chemical cluster approach (14, 15, 17, 18) using DFT to optimize the positions of heavy atoms (with hydrogens added where necessary) in key fragments of the ^{3min}HI-6•sarin–*m*AChE complex. To preserve the milieu of the protein interior, while reducing the number of atoms to a level compatible with quantum mechanical calculations, all atoms beyond the ^{3min}HI-6•sarin–*m*AChE interface were disregarded or prevented from moving during optimization by fixing their coordinates. Selected atoms in the vicinity of the sarin adduct (58–59 atoms) were allowed to move during these optimizations. ^{3min}HI-6•sarin–*m*AChE systems comprising 280–281 atoms in total were optimized using DFT (Table S2 and S3). The resulting atomic coordinates were visually compared with the experimentally determined electron densities.

To obtain a final structure of the complex, the DFT optimizations were integrated with the crystallographic refinements. Several alternative systems with different coordinates and protonation states for atoms with positions that could not be unambiguously determined from the electron densities of the initial crystallographic model were subjected to DFT geometry optimization. The conformations obtained by DFT were then used as input coordinates in a second round of crystallographic refinement processes. By iteratively performing DFT optimizations and crystallographic refinements in this way, a model was obtained that both converged in the DFT optimizations and was consistent with the experimental electron density maps. The deposited crystal structure (PDB ID code 5FPP) was generated in the final set of crystallographic refinements and includes both the *E* and *Z* isomers of the oxime.

Plausible Near-Attack Conformation of HI-6 and a Previously Undescribed Conformation of Sarin. The final structure generated by DFT calculations and crystallographic refinements includes a previously undescribed conformation of the sarin adduct featuring an interaction between the isopropyl moiety of sarin and the oxygens of Glu202 (Fig. 3 *A*–*C*). The sarin conformation provides space around the phosphorus atom, which is thus exposed to both isomers of the HI-6 oxime (Fig. 3 *A* and *B*). The oxygen of the *E* isomer is within van der Waals contact distance (3.3 Å) of the sarin phosphorus atom. The carboxy amino-substituted pyridinium ring of HI-6 forms a sandwich with the arenes of Tyr124 and Trp286 similar to that described previously (6).

Key interactions involving HI-6 and/or the sarin adduct in the active site were investigated by computing the gas-phase interaction energies (ΔE_{gas}) of suitable fragment systems using dispersion-corrected DFT (Fig. 3*D* and Fig. S2). The interactions between the sarin adduct and the *E*- and *Z*-oxime isomers were attractive; both isomers yielded similar interaction energies, regardless of their protonation state. The calculations also indicated that, for the studied fragments, the protonated forms of the oxime were energetically more favorable than the deprotonated forms. The interactions formed by the Ser203–sarin conjugate to Glu202 were also attractive, with interaction energies between −16.0 and −14.2 kcal/mol. The conformation of the sarin adduct seems to be stabilized by a nonclassical CH···O hydrogen bond formed between the isopropyl of sarin and the carboxylic acid of Glu202, with an interaction energy of ∼7 kcal/mol (Fig. S3 and S4 and Table S4). The interaction strength of the CH···O hydrogen bond is in accordance with the energy of previous identified nonclassical hydrogen bonds in AChE–ligand complexes (14).

In previously determined binary and ternary structures of *m*AChE phosphonylated by sarin, the *O*-isopropyl moiety of the sarin adduct was aligned along the axis of the active site gorge in a conformation that sterically shielded the sarin phosphorus against nucleophilic attack by the antidote. In contrast to the structure presented here, the side chain of Glu202 did not interact directly with the sarin moiety; instead, it was coordinated to a water molecule that acted as a bridge between Glu202 and the sarin O2 atom (6, 10, 19, 20). To further investigate the sarin adduct's conformation,

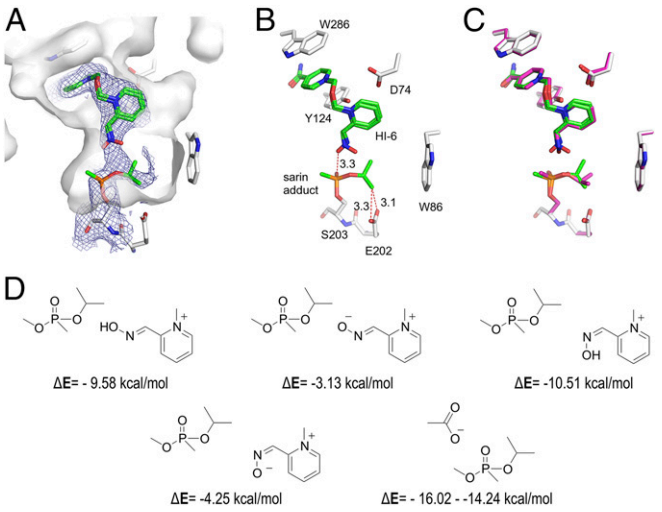

Fig. 3. (*A*) The final structure (sarin and HI-6 are shown in green) and the electron density map ($2F_o - F_c$ at 1σ shown in blue). The binding of the *E* and *Z* isomers of HI-6 to sarin–*m*AChE positions the nucleophilic oxime moiety close to the phosphorous atom of sarin. (*B*) Heavy atom distances are indicated as dashed lines. (*C*) Comparison of the final structure (green) and the conventionally refined structure (magenta). (*D*) The calculated interaction energies for selected fragments in gas phase calculated using the BLYP-D3/aug-cc-pVTZ method. For the interaction between Glu202 and the Ser203–sarin conjugate, the interaction energies in gas phase were calculated for the geometries obtained from the DFT geometry optimizations of all four complexes. In the figure, oxygen, nitrogen, and phosphorus are shown in red, blue, and orange, respectively.

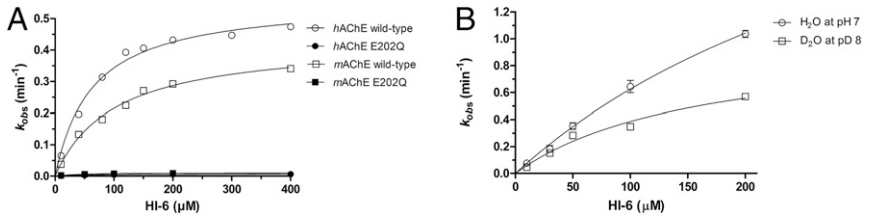

Fig. 4. (*A*) Reactivation kinetics of WT- and E202Q-substituted mouse and human AChE. (*B*) The solvent kinetic isotope effect of *h*AChE at optimal pH and pD.

we determined the structure of the binary complex formed by sarin and *Homo sapiens* acetylcholinesterase (*h*AChE; sarin–*h*AChE), which has a different space group than *m*AChE (Table S1). A superposition of sarin–*h*AChE and sarin–*m*AChE showed that the *O*-isopropyl group is positioned in a way that shields the phosphorus atom in both crystal forms, suggesting that the shielding conformation is a preferred conformer rather than merely being induced by crystal packing effects (Fig. S5).

Reactivation Kinetics Measurements Show the Importance of Glu202 and Reveal a Hydrogen Transfer Step. To clarify the role of Glu202 in the context of reactivation, the structure and interaction energy calculations were complemented with kinetic studies on HI-6's ability to reactivate AChE phosphonylated by sarin. Measurements of the reactivation kinetics of WT- and Glu202Asn-substituted mouse and human AChE showed that the mutation caused a 39- to 77-fold reduction of the reactivation rate in both the human and mouse enzymes (Fig. 4*A* and Table 1). However, the binding affinity of HI-6 to the phosphonylated enzyme was only marginally reduced by the mutation (1.1- to 2.6-fold). The large reduction in the reactivation rate and the negligible effect on the binding affinity support our finding that Glu202 has a key role in the reactivation process but little effect on the binding of HI-6. Thus, these results are consistent with the structure and interaction energy calculations, which suggested that Glu202 stabilizes the *O*-isopropyl moiety of the sarin adduct in a conformation that enables nucleophilic attack on the phosphorus atom by HI-6. Glu202 has previously been reported as a key residue of AChE with an important role in catalysis (21), phosphylation (22), and aging (23). Here, we also observed, in addition to the interaction with the *O*-isopropyl moiety, an interaction between Glu202 and the methylene of Ser203 with an interaction energy of ∼7 kcal/mol (Table S4).

To further investigate the reaction, its solvent kinetic isotope effect was measured in H_2O and D_2O using WT human AChE. If a transfer of one or more protons occurs in the rate-limiting step, the reaction rate in D_2O will be lower than in H_2O. However, both solvents will yield similar rates if the reaction only requires the complex to be in a particular protonation state (24). As shown in Fig. 4*B*, the rate in D_2O was lower than in H_2O. Furthermore, the reaction's pH optimum is 7.0, but its pD optimum is 8.0 (Fig. S6). Shifts in this direction are commonly observed for enzymatic reactions and reflect the difference between deuterium and protium ionization (24).

Multiple Binding Poses During HI-6–Assisted Reactivation. The structural and kinetic data for the ^{3min}HI-6•sarin–*m*AChE complex presented herein suggest a prereaction complex that agree with previously reported reactivation kinetics of site-directed mutants (ref. 25 and references therein) (Movie S1). Furthermore, in conjunction with the previously reported structures, the prereaction complex makes it possible to identify many of the chemical species and conformational changes that are involved in the reactivation cycle (Fig. 5).

The substrate of HI-6 is represented by the binary crystal structure of AChE inhibited by sarin (sarin–*m*AChE and sarin–*h*AChE). In these structures, the *O*-isopropyl moiety of sarin is directed toward the indole ring of Trp86 and interacts with Glu202 through a bridging interaction with a conserved water molecule (19). This pose is the preferred conformation of the sarin adduct in the crystal structures of both the human and mouse enzymes (Fig. S5).

The complex formed by the initial binding of HI-6 to the binary complex is assumed to correspond to the structure determined after 1 min of incubation in HI-6 (^{1min}HI-6•sarin–*m*AChE; PDB ID code 2WHP). The binding pose of the sarin adduct in this ternary complex is very similar to that of the binary complex: it retains the bridging water molecule between Glu202 and the sarin moiety, and the system's coordination is largely unaffected by the binding of HI-6 (6). However, there is a significant change in the conformation and position of Trp286 that allows the nonreactive carboxyamino-substituted pyridinium ring of HI-6 to form a sandwich with the arenes of Tyr124 and Trp286. This conformation of Trp286 is equivalent to the pose observed in the binary HI-6•*m*AChE (PDB ID code 2GYU). Another striking feature of the structure collected after a 1-min soak is its partially disordered electron density map, which suggests that the oxime-pyridinium of HI-6 is highly mobile, a conclusion also supported by molecular dynamics simulations (6).

The structure determined from data collected after a 3-min incubation (^{3min}HI-6•sarin–*m*AChE; PDB ID code 5FPP) and DFT calculations suggests that the *O*-isopropyl moiety of sarin undergoes a conformational change and forms a direct stabilizing interaction

Table 1. Reactivation kinetics and measurements of solvent kinetic isotope effect

	*h*AChE		*m*AChE	
	WT	E202Q	WT	E202Q
k_r (min^{-1})	0.56 (0.5–0.6)	0.0073 (0.007–0.008)	0.43 (0.38–0.48)	0.011 (0.010–0.012)
K_d (μM)	63 (43–83)	56 (43–70)	100 (69–130)	39 (24–54)
k_r/K_d (mM^{-1} min^{-1})	8.9	0.13	4.3	0.28
$^{H}k_r$ (min^{-1})*	3.1 (2.1–4.1)	N.D.	N.D.	N.D.
$^{D}k_r$ (min^{-1})†	1.0 (0.7–1.3)	N.D.	N.D.	N.D.

Values are means (95% confidence intervals). N.D., not determined.
*At pH optimum of 7.0 (Fig. S6).
†At pD optimum of 8.0 (Fig. S6).

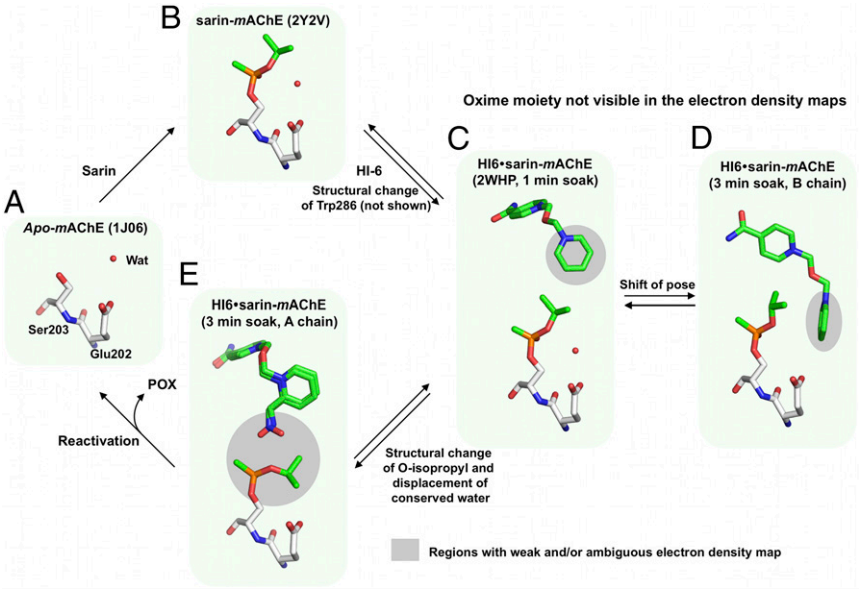

Fig. 5. Visualization of the reactivation cycle. (*A*) The *apo* form of the enzyme with a conserved water molecule within hydrogen bonding distance of Glu202. (*B*) Binary complex between sarin and *m*AChE. (*C*) The complex formed after a 1-min soak, showing the initial binding configuration of HI-6 in which the oxime-pyridinium moiety exhibits substantial conformational flexibility. (*D*) A nonproductive pose adopted by HI-6 in the B monomer of the asymmetric unit obtained after a 3-min soak. (*E*) The corresponding pose in the A monomer, which was determined by a combined crystallographic and DFT refinement. Oxygen, nitrogen, and phosphorus are shown in red, blue, and orange, respectively.

with Glu202, displacing the bridging water molecule. In addition, the oxime moiety is positioned apically within contact distance of the sarin phosphorus atom, oriented in a way that is consistent with a nucleophilic inline attack, although other mechanisms may be possible (26, 27).

The structure of the asymmetric unit's B monomer reveals a potential additional binding site for HI-6 close to Trp86 (Fig. S1). However, arene stacking interactions with Trp86 in this structure would place the nucleophile in an unfavorable position for reaction, and therefore, it probably represents an unproductive HI-6 binding pose.

The proposed scheme implies that the carboxylic acid of Glu202 acts as a hydrogen bond acceptor that stabilizes the sarin *O*-isopropyl moiety through a CH···O hydrogen bond. The kinetics measurements indicate that the Glu202Asn substitution reduces the rate constant of the reactivation reaction by a factor of 30–80 but has only a marginal effect on the dissociation constant (Fig. 4*A* and Table 1). The significant reduction of the rate constant supports the hypothesis that Glu202 stabilizes the adduct in an oxime-accessible conformation, whereas the small effect on the dissociation constant indicates that Glu202 does not directly influence the binding of HI-6. These findings are consistent with the ^{3min}HI-6•sarin–*m*AChE structure and earlier studies of Glu202 substitutions (25, 28).

We have previously suggested that His447 and a water molecule activate the oxime by a hydrogen transfer mechanism to generate a deprotonated species that is presumed to attack the phosphorus atom (6, 29). This proposal has been challenged by kinetics data, which suggested that the oxime binds in its deprotonated form (30). The potential transfer of a hydrogen was investigated by measuring the solvent kinetic isotope effect during HI-6–assisted reactivation of AChE inhibited by sarin (Fig. 4*B* and Table 1). The ratio of the rate constants in H_2O and D_2O ($^{H}k_r/^{D}k_r$) was 3.1, indicating that a hydrogen transfer occurs close to the rate-limiting step. The most likely acceptor is His447, possibly assisted by a water molecule.

The presented reactivation cycle (Fig. 5) shows multiple structurally distinct conformations that call for a review and maybe an expansion of the currently used kinetic models. In addition, it opens up for new approaches in computational design of new antidotes, including attempts to shift the equilibrium to favor productive prereactive conformations.

Conclusions

Recent advances in methods for preserving and analyzing conformational ensembles together with computational approaches for extracting alternative protein and ligand conformations have made it possible to use X-ray crystallography to investigate rare conformations and molecular motions (12, 13, 31, 32). Here, we have combined diffusion trap cryocrystallography and DFT calculations to generate and analyze crystallographic data for a system comprising the nerve agent sarin, its biological target AChE, and the therapeutic antidote HI-6. This system is inherently complex and challenging to study using conventional crystallographic approaches. We present a structure that is consistent with our DFT calculations and the reactivation kinetics. The structure shows a previously unknown conformation of the sarin adduct that allows the nucleophilic oxime moiety of HI-6 to approach and bind close to the sarin adduct's phosphorus atom, with the carboxylic group of Glu202 stabilizing the adduct in the oxime-accessible conformation. The importance of this interaction is supported by a Glu202Asn substitution that reduces the rate of reactivation by factors of 39 and 77 in *m*AChE and *h*AChE, respectively. Solvent isotope effect measurements show a decreased reaction rate and an increase in pL optimum ($L = D$ or H) when H_2O is exchanged for D_2O, suggesting that a hydrogen transfer occurs close to the rate-limiting step.

As illustrated herein, the integration of DFT calculations with X-ray crystallography is a powerful combination that provides unexplored possibilities for computational chemistry and structural biology. The combination of techniques allowed us to determine a structure that may provide a starting point for analysis of reaction pathways and structure-based design of improved nerve agent antidotes.

Materials and Methods

Detailed information on the methods is provided in *SI Materials and Methods*.

Protein Expression and X-Ray Crystallography. *m*AChE and *h*AChE were expressed in HEK293F cells and purified using affinity and size exclusion chromatography. Protein crystallization was done by the hanging drop vapor diffusion method. HI-6•sarin–*m*AChE complexes were generated using a diffusion trap approach, and data were collected at beamlines I911-3 and I911-2 at Max Laboratory. Initial crystallographic refinement was performed using conventional methods, whereas the late-stage refinement included DFT geometry optimizations, focusing on areas within the active site that showed ambiguous electron density maps.

Computational Methods. All-atom protein models were prepared from the X-ray coordinates of ^{3min}HI-6•sarin–*m*AChE. The systems were thereafter reduced, and a chemical cluster approach (14, 15, 17, 18) was adopted, where subsets of the atoms were fully flexible during geometry optimization using implicitly dispersion-corrected DFT [M06-2X (33) /6–31G**]. After additional reduction of the systems, interaction energies (ΔE_{gas}) were calculated around selected fragments (molecule pairs) using BLYP-D3/aug-cc-pVTZ (14). The calculations were run at the High Performance Computing Center North (www.hpc2n.umu.se).

Reactivation Kinetics and Data Analysis. The enzymatic activity of *h*AChE and *m*AChE was inhibited by a molar excess of sarin. After verification of enzyme inhibition and lack of residual inhibitor activity, different concentrations of HI-6 were added, and the percentage of reactivation as a function of time and HI-6 concentration was determined. Measurements were done in both H_2O and D_2O, and the enzyme activity was determined by a modified Ellman assay (34).

ACKNOWLEDGMENTS. We thank Dr. Brian Bennion and Dr. Jure Stojan for fruitful discussions and critical comments on the manuscript. We also thank the MX beamline staff at the MAXlab Synchrotron Facility for excellent assistance and the High Performance Computing Center North for computational resources and technical support.

1. Frauenfelder H, Petsko GA, Tsernoglou D (1979) Temperature-dependent X-ray diffraction as a probe of protein structural dynamics. *Nature* 280(5723):558–563.
2. Frauenfelder H, Sligar SG, Wolynes PG (1991) The energy landscapes and motions of proteins. *Science* 254(5038):1598–1603.
3. Ringe D, Petsko GA (1985) Mapping protein dynamics by X-ray diffraction. *Prog Biophys Mol Biol* 45(3):197–235.
4. Wilson IB, Ginsburg B (1955) A powerful reactivator of alkylphosphate-inhibited acetylcholinesterase. *Biochim Biophys Acta* 18(1):168–170.
5. Luo C, et al. (1999) Phosphoryl oxime inhibition of acetylcholinesterase during oxime reactivation is prevented by edrophonium. *Biochemistry* 38(31):9937–9947.
6. Ekström F, et al. (2009) Structure of HI-6*sarin-acetylcholinesterase determined by X-ray crystallography and molecular dynamics simulation: Reactivator mechanism and design. *PLoS One* 4(6):e5957.
7. Harris LW, Fleisher JH, Clark J, Cliff WJ (1966) Dealkylation and loss of capacity for reactivation of cholinesterase inhibited by sarin. *Science* 154(3747):404–407.
8. Wilson IB, Ginsburg S (1959) Reactivation of alkylphosphate inhibited acetylcholinesterase by bis quaternary derivatives of 2-PAM and 4-PAM. *Biochem Pharmacol* 1(3): 200–206.
9. Millard CB, et al. (1999) Reaction products of acetylcholinesterase and VX reveal a mobile histidine in the catalytic triad. *J Am Chem Soc* 121(42):9883–9884.
10. Millard CB, et al. (1999) Crystal structures of aged phosphonylated acetylcholinesterase: Nerve agent reaction products at the atomic level. *Biochemistry* 38(22): 7032–7039.
11. de Jong LP, Wolring GZ (1984) Stereospecific reactivation by some Hagedorn-oximes of acetylcholinesterases from various species including man, inhibited by soman. *Biochem Pharmacol* 33(7):1119–1125.
12. Fraser JS, et al. (2009) Hidden alternative structures of proline isomerase essential for catalysis. *Nature* 462(7273):669–673.
13. Lang PT, Holton JM, Fraser JS, Alber T (2014) Protein structural ensembles are revealed by redefining X-ray electron density noise. *Proc Natl Acad Sci USA* 111(1): 237–242.
14. Berg L, Mishra BK, Andersson CD, Ekström F, Linusson A (2016) The nature of activated non-classical hydrogen bonds: A case study on acetylcholinesterase-ligand complexes. *Chemistry* 22(8):2672–2681.
15. Berg L, et al. (2012) Similar but different: Thermodynamic and structural characterization of a pair of enantiomers binding to acetylcholinesterase. *Angew Chem Int Ed Engl* 51(51):12716–12720.
16. Ryde U, Olsen L, Nilsson K (2002) Quantum chemical geometry optimizations in proteins using crystallographic raw data. *J Comput Chem* 23(11):1058–1070.
17. Siegbahn PE, Himo F (2009) Recent developments of the quantum chemical cluster approach for modeling enzyme reactions. *J Biol Inorg Chem* 14(5):643–651.
18. Siegbahn PEM, Himo F (2011) The quantum chemical cluster approach for modeling enzyme reactions. *WIREs Comput Mol Sci* 1(3):323–336.
19. Hörnberg A, Tunemalm AK, Ekström F (2007) Crystal structures of acetylcholinesterase in complex with organophosphorus compounds suggest that the acyl pocket modulates the aging reaction by precluding the formation of the trigonal bipyramidal transition state. *Biochemistry* 46(16):4815–4825.
20. Koellner G, et al. (2000) Active-site gorge and buried water molecules in crystal structures of acetylcholinesterase from Torpedo californica. *J Mol Biol* 296(2):713–735.
21. Malany S, et al. (1999) Theoretical and experimental investigations of electrostatic effects on acetylcholinesterase catalysis and inhibition. *Chem Biol Interact* 119-120: 99–110.
22. Radić Z, et al. (1992) Expression of recombinant acetylcholinesterase in a baculovirus system: Kinetic properties of glutamate 199 mutants. *Biochemistry* 31(40):9760–9767.
23. Saxena A, et al. (1993) The role of glutamate-199 in the aging of cholinesterase. *Biochem Biophys Res Commun* 197(1):343–349.
24. Smith MD, Collins RA (2007) Evidence for proton transfer in the rate-limiting step of a fast-cleaving Varkud satellite ribozyme. *Proc Natl Acad Sci USA* 104(14):5818–5823.
25. Chambers C, Luo C, Tong M, Yang Y, Saxena A (2015) Probing the role of amino acids in oxime-mediated reactivation of nerve agent-inhibited human acetylcholinesterase. *Toxicol In Vitro* 29(2):408–414.
26. Hall CR, Inch TD (1980) Phosphorus stereochemistry: Mechanistic implications of the observed stereochemistry of bond forming and breaking processes at phosphorus in some 5- and 6-membered cyclic phosphorus esters. *Tetrahedron* 36(14):2059–2095.
27. Ashani Y, et al. (1995) Amino acid residues controlling reactivation of organophosphonyl conjugates of acetylcholinesterase by mono- and bisquaternary oximes. *J Biol Chem* 270(11):6370–6380.
28. Grosfeld H, Barak D, Ordentlich A, Velan B, Shafferman A (1996) Interactions of oxime reactivators with diethylphosphoryl adducts of human acetylcholinesterase and its mutant derivatives. *Mol Pharmacol* 50(3):639–649.
29. Hörnberg A, Artursson E, Wärme R, Pang YP, Ekström F (2010) Crystal structures of oxime-bound fenamiphos-acetylcholinesterases: Reactivation involving flipping of the His447 ring to form a reactive Glu334-His447-oxime triad. *Biochem Pharmacol* 79(3):507–515.
30. Radić Z, Kalisiak J, Fokin VV, Sharpless KB, Taylor P (2010) Interaction kinetics of oximes with native, phosphylated and aged human acetylcholinesterase. *Chem Biol Interact* 187(1-3):163–166.
31. Fraser JS, et al. (2011) Accessing protein conformational ensembles using room-temperature X-ray crystallography. *Proc Natl Acad Sci USA* 108(39):16247–16252.
32. Oksanen E, Blakeley MP, El-Hajji M, Ryde U, Budayova-Spano M (2014) The neutron structure of urate oxidase resolves a long-standing mechanistic conundrum and reveals unexpected changes in protonation. *PLoS One* 9(1):e86651.
33. Zhao Y, Truhlar DG (2008) The M06 suite of density functionals for main group thermochemistry, thermochemical kinetics, noncovalent interactions, excited states, and transition elements: two new functionals and systematic testing of four M06-class functionals and 12 other functionals. *Theor Chem Acc* 120(1-3):215–241.
34. Ellman GL, Courtney KD, Andres V, Jr, Feather-Stone RM (1961) A new and rapid colorimetric determination of acetylcholinesterase activity. *Biochem Pharmacol* 7: 88–95.
35. Artursson E, Akfur C, Hörnberg A, Worek F, Ekström F (2009) Reactivation of tabun-hAChE investigated by structurally analogous oximes and mutagenesis. *Toxicology* 265(3):108–114.
36. Ekström F, Akfur C, Tunemalm AK, Lundberg S (2006) Structural changes of phenylalanine 338 and histidine 447 revealed by the crystal structures of tabun-inhibited murine acetylcholinesterase. *Biochemistry* 45(1):74–81.
37. Cheung J, et al. (2012) Structures of human acetylcholinesterase in complex with pharmacologically important ligands. *J Med Chem* 55(22):10282–10286.
38. Kabsch W (1988) Evaluation of single-crystal X-ray diffraction data from a position-sensitive detector. *J Appl Crystallogr* 21(6):916–924.
39. Murshudov GN, Vagin AA, Dodson EJ (1997) Refinement of macromolecular structures by the maximum-likelihood method. *Acta Crystallogr D Biol Crystallogr* 53(Pt 3): 240–255.
40. Emsley P, Cowtan K (2004) Coot: model-building tools for molecular graphics. *Acta Crystallogr D Biol Crystallogr* 60(Pt 12):2126–2132.
41. Adams PD, et al. (2002) PHENIX: Building new software for automated crystallographic structure determination. *Acta Crystallogr D Biol Crystallogr* 58(Pt 11): 1948–1954.
42. Berman HM, et al. (2000) The Protein Data Bank. *Nucleic Acids Res* 28(1):235–242.
43. Schrödinger (2010) Maestro (Schrödinger LLC, New York), Version 9.1.
44. Schrödinger (2010) Prime (Schrödinger LLC, New York), Version 2.2.
45. Halgren TA (1999) MMFF VI. MMFF94s option for energy minimization studies. *J Comput Chem* 20(7):720–729.
46. Halgren TA (1999) MMFF VII. Characterization of MMFF94, MMFF94s, and other widely available force fields for conformational energies and for intermolecular-interaction energies and geometries. *J Comput Chem* 20(7):730–748.
47. Schrödinger (2010) Macromodel (Schrödinger LLC, New York), Version 9.8.
48. Schrödinger (2011) Jaguar (Schrödinger LLC, New York), Version 7.8.